Materials Advances

ROYAL SOCIETY OF CHEMISTRY

PAPER

View Article Online
View Journal | View Issue

Cite this: *Mater. Adv.*, 2024, 5, 4902

A self-assembled Ru nanozyme with H_2O_2-activated oxygenation for NIR-II photoacoustic imaging-guided photothermal/photodynamic therapy†

Guang Liu,‡ Zhilang Li,‡ Zirong Lv,‡ Qiuping Zheng, Cunji Gao, * Jianniao Tian and Xing-Can Shen *

Received 2nd February 2024,
Accepted 22nd April 2024

DOI: 10.1039/d4ma00103f

rsc.li/materials-advances

The characteristic hypoxia of solid tumors seriously reduced the treatment efficacy of oxygen-dependent photodynamic therapy (PDT). Herein, an oxygen nanogenerator, comprising Ru-based nanomaterials, CS–DA@Ru nanoparticles (NPs), has been constructed to relieve tumor hypoxia along with photodynamic/photothermal therapy for efficient tumor eradication. CS–DA@Ru NPs possess targeting ability and act as catalase-mimic nanozymes to decompose endogenous hydrogen peroxide in the tumor to produce O_2. The broad absorbance of CS–DA@Ru NPs in the second near-infrared (NIR-II) region enabled them to possess good photothermal properties and photoacoustic (PA) imaging ability. CS–DA@Ru NPs could generate enough hyperthermia and enormous amounts of $^1O_2$ under NIR-II laser irradiation. Specifically, CS–DA@Ru NPs exhibit catalase-like activity as well as a significantly augmented antitumor efficacy through synergistic PTT/PDT guided by NIR-II PA imaging in both cells and *in vivo* experiments. This work will advance the development of noble metal nanozymes in enhancing the efficacy of O_2-dependent antitumor modalities.

Introduction

Photodynamic therapy (PDT) has been widely explored over the past few decades since it utilizes near-infrared (NIR) light to illuminate photosensitizers (PSs) and transforms surrounding oxygen to generate highly cytotoxic singlet oxygen ($^1O_2$) to kill cancer cells.[1–3] By virtue of the spatiotemporal management of the NIR light irradiation location, PDT can significantly augment treatment efficacy and remarkably reduce side effects. Compared with conventional radiotherapy, chemotherapy, and surgery, PDT possesses many advantages including minimal invasiveness, spatiotemporal precision, and avoidance of drug resistance.[4,5] The tumor microenvironment (TME) has many characteristics that are different from normal tissues, such as mild acidity, H_2O_2 overproduction and hypoxia.[6] Therefore, O_2-dependent PDT efficacy is seriously reduced because solid tumors suffer from hypoxia resulting from the uncontrollable tumor growth and the dysregulated tumor blood vessels.[7,8] To date, three main strategies have been developed to address tumor hypoxia to enhance the effects of oxygen-dependent antitumor modalities, including (1) the use of hemoglobin-based oxygen delivery vectors to directly deliver O_2 to the tumor region,[9,10] (2) the use of selective nanoplatforms such as CaO_2 for *in situ* production of O_2 in tumors,[11] (3) the development of catalytic nanomaterials for *in situ* O_2 generation through catalysis of the decomposition of endogenous overproduced H_2O_2 into O_2.[12,13] Due to the high level of H_2O_2 in the tumor microenvironment, designing smart nanoplatforms for localized production of O_2 in tumors has become one of the popular strategies.[14–16] Many nanomaterials with catalase (CAT) activities have been constructed as smart nanoplatforms to catalyze intracellular H_2O_2 to O_2 in tumors, such as MnO_2,[17] carbon dots,[18] and Au@Pt core–shell nanomaterials.[19] Although these strategies have significantly improved tumor hypoxia, there is still a need to develop catalytic nanomaterials to decompose endogenous H_2O_2 into O_2.

Recently, Ru-based nanomaterials have been constructed by researchers for cancer therapy because of their superior catalytic performance.[20–22] They could decompose endogenous overproduced H_2O_2 into O_2 to relieve tumor hypoxia and then improve the effect of photodynamic therapy. For example, our group has developed hyaluronic acid-hybridized Ru nanoaggregates (HA–

State Key Laboratory for Chemistry and Molecular Engineering of Medicinal Resources, Key Laboratory for Chemistry and Molecular Engineering of Medicinal Resources (Ministry of Education of China), Collaborative Innovation Center for Guangxi Ethnic Medicine, School of Chemistry and Pharmaceutical Sciences, Guangxi Normal University, Guilin 541004, People's Republic of China.
E-mail: gaocj@mailbox.gxnu.edu.cn, xcshen@mailbox.gxnu.edu.cn

† Electronic supplementary information (ESI) available. See DOI: https://doi.org/10.1039/d4ma00103f

‡ Guang Liu, Zhilang Li, and Zirong Lv contributed equally to this work.

Ru NAs) with CAT activity for enhanced photothermal and photodynamic therapy *via* TME responsiveness.[23] Furthermore, Ru-based nanomaterials with good photothermal conversion efficiency make them act as photothermal agents for photothermal therapy (PTT), further enhancing the therapeutic effect through the combination of PDT/PTT. However, the absorption of these Ru-based nanomaterials is located in the first NIR region (NIR-I, 650–900 nm) with poor penetration depth. The second NIR region (NIR-II, 1000–1700 nm) has a higher penetration depth and signal-to-noise ratio owing to its lower background absorption and scattering.[24–26] On the basis of these merits of NIR-II region light, NIR-II photoacoustic (PA) imaging has been extensively employed to guide photodynamic and photothermal therapy.[27,28] Therefore, developing NIR-II light-mediated Ru-based photosensitizers with CAT activity and good photothermal conversion efficiency is required and still remains a challenge.

Chondroitin sulfate (CS) is an anionic heteropolysaccharide derived from sulfated glycosaminoglycans, which has many biological functions exhibiting anti-oxidant, anti-inflammatory, anti-tumor properties *etc.*[29,30] Recently, it has been found to have the ability of active targeting owing to its high affinity for CD44 receptors, which are overexpressed on the cancer cells surface. As the CS–CD44 interaction triggers endocytosis, this behavior can be used to introduce nanomaterials conjugated or adsorbed to CS into cancer cells.[31] In particular, CS possesses great potential as an encrustation coating due to its negative charge and strong hydrophilicity.[32] Therefore, the development of NIR-II-responsive Ru nanoparticles with a stable encrustation coating for cancer treatment is a major advancement.

Based on this, in this study, we synthesized CS–DA@Ru NPs *via* self-assembly for NIR-II PA imaging-guided combination of PDT/PTT (Scheme 1). Due to the reduction of dopamine (DA), CS–DA reduced $RuCl_3$ to Ru NPs and CS–DA@Ru NPs were formed. The CS–DA@Ru NP nanozyme with CAT activity could catalyze endogenous overexpressed H_2O_2 to generate O_2 in tumors, achieving *in situ* self-supplying O_2 to relieve tumor hypoxia. The CS–DA@Ru NP nanozyme exhibits good water dispersibility and stability under physiological conditions. CS–DA@Ru NPs possess broad NIR-II area absorption, good photothermal properties, and active targeting ability. CS–DA@Ru NPs could generate enough hyperthermia and enormous amounts of $^1O_2$ using 1064 nm laser illumination. Both *in vitro* and *in vivo* experiments confirmed that the synthesized CS–DA@Ru NPs effectively suppressed tumor growth owing to the combination effect of PDT/PPT. This study broadens the applications of Ru-based nanomaterials in cancer imaging and highly effective treatment by modulating the tumor microenvironments.

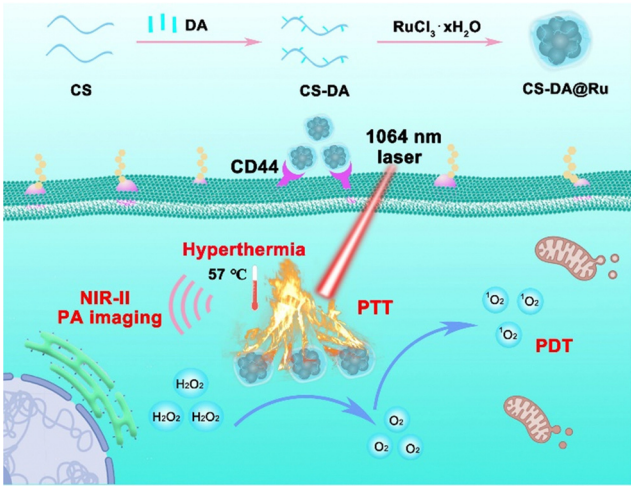

Scheme 1 Schematic illustration of the main synthesis procedure of CS–DA@Ru NPs, and NIR-II-mediated ROS generation and hyperthermia for PTT/PDT.

Experimental section

Materials

Chondroitin 4-sulfate sodium salt (CS), dopamine (DA), ruthenium chloride hydrate ($RuCl_3{\cdot}xH_2O$), *N*-hydroxysuccinimide (NHS), and 1-(3-dimethylaminopropyl)-3-ethylcarbodiimide methiodide (EDC) were purchased from Aladdin Biochemical Technology Co., Ltd (Shanghai, China). Hydrogen peroxide (H_2O_2) and dimethyl sulfoxide (DMSO) were purchased from Xilong Chemical Co., Ltd (Guangzhou, China). 1,3-Diphenylisobenzofuran (DPBF), propidium iodide (PI), 3-(4,5-dimethylthiazol-2-yl)-2,5-diphenyltetrazolium bromide (MTT), 2,7-dichloro-dihydro-fluorescein diacetate (DCFH-DA), 4-amino-2,2,6,6-tetramethylpiperidine (TEMP) calcein-AM, and trypsin were purchased from Sigma-Aldrich Chemical Co., Ltd (Milwaukee, WI, USA). Foetal bovine serum (FBS) was obtained from HyClone (USA). RPMI-1640 medium and DMEM were purchased from Gibco (Shanghai, China). Murine fibroblast normal cells (L929), murine breast cancer cells (4T1), and human cervical cancer cells (HeLa) were purchased from the Chinese Academy of Sciences Cell Bank (Kunming, China). All reagents were obtained from commercial sources and used as received.

Preparation of CS–DA@Ru NPs

CS (250 mg) was dissolved in deionized water (20 mL). EDC (138 mg) and NHS (83 mg) were dissolved in 20 mL of DMSO. Then, it was added to the above prepared CS solution and reacted at 25 °C for 30 min. DA (114 mg) was dissolved in 10 mL of DMSO and then added to the above solution. The pH of the solution was adjusted to 5.00 using hydrochloric acid and stirred at 25 °C under a nitrogen atmosphere for 24 h. Finally, the obtained solution was dialyzed in a dialysis bag (MW = 3500 Da) for 96 h and freeze-dried to obtain CS–DA.

$RuCl_3{\cdot}xH_2O$ (5 mg) was dissolved in deionized water (50 mL). CS–DA (50 mg) was added and stirred at 80 °C for 12 h. The as-prepared solution was dialyzed in a dialysis bag (MW = 3500 Da) for 72 h and freeze-dried to obtain CS–DA@Ru NPs.

Characterization

UV-vis-NIR spectra were measured at 400–1200 nm employing a UV2600 UV-vis spectrometer (Shimadzu, Japan). FTIR spectra were recorded employing an FTIR spectrometer (PerkinElmer, USA).

The morphologies of CS–DA–Ru NPs were observed using a Talos F200S microscope (Thermo Fisher Scientific, USA). X-ray diffraction (XRD) analysis was measured using a Rigaku D/MAX 2500 v/pc diffractometer (Rigaku, Japan). Zeta potential and dynamic light scattering (DLS) were recorded employing a Malvern Zetasizer NanoZS potentiometer (Malvern, UK). X-ray photoelectron spectra (XPS) were measured employing an ESCALAB 250Xi spectrometer (Thermo Fisher Scientific). The temperature changes were recorded using a MAG30 infrared thermal imager.

Determination of the photothermal effect of CS–DA@Ru NPs

To estimate the photothermal property of CS–DA@Ru NPs, 0.5 mL of CS–DA–Ru NPs aqueous solution of different concentrations (0, 25, 50, 100, 150, and 200 μg mL^{-1}) were illuminated using a 1064 nm laser (1.0 W cm^{-2}) for 600 s at room temperature, and an IR thermal camera was employed to photograph and record the temperature change of the CS–DA@Ru NPs solution. Water was also irradiated using the same conditions for comparison. To estimate the photothermal stability of CS–DA@Ru NPs, a CS–DA@Ru NPs (200 μg mL^{-1}) solution was illuminated using a 1064 nm laser for 600 s, and the laser was then turned off until the temperature of the CS–DA@Ru NPs solution decreased to 25 °C. This process was repeated five times.

ROS detection

A solution of DPBF (50 μL, 1.0 mg mL^{-1}) in DMF was put into 3 mL of CS–DA@Ru NPs solution. Then, H_2O_2 (30 μL, 10 mM) was added. The mixture was illuminated using 1064 nm light (1.0 W cm^{-2}) for different times (0, 2, 4, 6, 8, and 10 min). The UV-vis absorption of DPBF was tested at different intervals. For DPBF under 1064 nm light irradiation, CS–DA@Ru NPs + DPBF was set as the control groups.

Cellular targeting ability of CS–DA@Ru NPs detection

L929, 4T1 and HeLa cells were inoculated into 6-well plates (1.0×10^5 cells per well). After being incubated in the medium for 12 h, the medium was removed and fresh medium was added. The CS solution was added to the control group for 2 h, then the CS–DA@Ru NPs solution was added to the control and experimental groups and its final concentration was 200 μg mL^{-1}. The cells were incubated for 1, 2, 3, 4, 5, and 6 h. The cells incubated for different times were washed three times with PBS to remove excess CS–DA@Ru NPs. Then the cells were digested and collected from the plate using trypsin. Finally, the cells were immersed in HNO_3 for 24 h, and the content of Ru in the solution was detected by ICP-MS to analyze the cell targeting ability of CS–DA–Ru NPs.

In vitro ROS detection

The DCFH-DA probe was employed to determine the ROS production capability *in vitro*. 4T1, HeLa, and L929 cells were seeded into 24-well plates. After 24 h of incubation, a CS–DA–Ru NPs solution was added and its final concentration was 200 μg mL^{-1}. The cells were cultured at 37 °C for 6 h in the dark. Then DCFH-DA was added with the final concentration of 10 μM. The cells were incubated for 30 min and then washed with PBS three times. The cells were illuminated using 1064 nm light for 300 s. Finally, the cells were imaged using a multifunctional microscopic reader (SynergyH1, BioTek).

In vitro cytotoxicity of CS–DA@Ru NPs

Cell viability was estimated employing a standard MTT assay. In detail, HeLa, 4T1, and L929 cells (1.0×10^5 cells per well) were seeded in a 96-well plate and treated for 24 h. 20 μL of CS–DA@Ru NPs solution with different concentrations was added to each well, resulting in final concentrations of 0, 25, 50, 100, 150, and 200 μg mL^{-1}. The same volume of PBS was added in the control group. After 12 h of incubation, the cells were washed with PBS (200 μL) three times. Fresh medium (200 μL) was added to each well. Subsequently, the MTT solution (10 μL) was added to each well and the cells were cultured for 4 h. The medium was discarded, and DMSO (100 μL) was added. The plate was shocked until formazan was completely dissolved. Cell viability was measured by testing the absorbance at 570 and 630 nm on a microplate reader (SynergyH1, BioTek). The cell-killing efficacy of CS–DA@Ru NPs with 1064 nm light illumination was also evaluated in 4T1, HeLa, and L929 cells using the standard MTT assay. The procedure was similar to that employed to estimate the biocompatibility of CS–DA@Ru NPs. After 4 h of incubation, the medium was removed, and fresh medium was added. The cells were illuminated with 1064 nm light (1.0 W cm^{-2}) for 300 s. After another 2 h of incubation, cell viability was examined as described above.

Live/dead cell staining assay

Calcein-AM and PI were employed to estimate the number of live and dead cells, respectively. HeLa, 4T1, and L929 cells (1.0×10^5 cells per well) were put in a 96-well plate and incubated for 24 h. They were treated with CS–DA@Ru NPs (200 μg mL^{-1}) and incubated for 4 h. Next, the cells were illuminated with 1064 nm light for 10 min. The cells were washed three times with PBS. After that, fresh culture medium was added. Next, 2 μL of PI (2 μM) and 2 μL of calcein-AM (1 μM) were added to each plate and cultured for 20 min. The cells were washed with PBS three times. Living and dead cells were imaged employing a microplate reader (SynergyH1, BioTek).

Establishment of an animal model

Female BALB/c nude mice (6–7 weeks) weighing approximately 20 g were obtained from Hunan SJA Laboratory Animal Co., Ltd and employed to build the tumor model. PBS (100 μL) containing 4T1 cells (1×10^7 cells mL^{-1}) was injected subcutaneously into the right limb of each mouse. Subsequently, the experiments were carried out when the tumor volume reached approximately 70–80 mm^3. All *in vivo* experimental procedures were performed in accordance with the guidelines of the Experimental Animal Center of Guangxi Normal University (no. 2024-01-002).

In vitro and *in vivo* PA imaging

First, the CS–DA@Ru NPs solution with different concentrations (25, 50, 100, 150, and 200 μg mL^{-1}) was used to obtain an *in vitro* PA signal. For *in vivo* PA imaging, the CS–DA@Ru NPs solution (100 μL, 2.0 mg mL^{-1}) was intravenously (i.v.) administrated into the 4T1 tumor-bearing BALB/c nude mice. Next, we imaged the tumor site using a MSOT (multispectral optoacoustic tomography) imaging system at different times (0, 4, 8, 12, 24, and 48 h).

Detection of saturated oxygen level in tumor vessels

The CS–DA@Ru NPs solution (100 μL, 2.0 mg mL^{-1}) was i.v. administrated into the 4T1 tumor-bearing nude mice. Subsequently, we imaged the tumor site using a MSOT imaging system at different times (0, 4, 8, 12, 24, and 48 h). All results are analyzed using the View MSOT software. The PA imaging was reconstructed employing the model linear method, and the spectrum at 850 nm was used to monitor and separate the signals from hypoxic hemoglobin (Hb) and oxygenated hemoglobin (HbO_2).

In vivo photothermal imaging

The CS–DA@Ru NPs solution (100 μL, 2.0 mg mL^{-1}) was i.v. injected into the mice *via* the tail. The control group was i.v. administrated with saline (100 μL) through the tail. After 12 h of injection, the tumors were irradiated with 1064 nm light (1.0 W cm^{-2}) for 300 s. Next, we recorded the temperature changes of the tumor site using an infrared thermal camera during the irradiation process.

In vivo antitumor efficacy evaluation of CS–DA@Ru NPs

To estimate the antitumor efficacy of CS–DA@Ru NPs in mice, thirty 4T1 tumor-bearing BALB/c nude mice were randomly separated into four groups (n = 5): (1) saline, (2) saline + 1064 nm laser, (3) CS–DA@Ru NPs, and (4) CS–DA@Ru NPs + 1064 nm laser. 100 μL of saline and 100 μL of CS–DA@Ru NPs (2.0 mg mL^{-1}) were i.v. administered into mice. After 12 h of injection, the tumor site was irradiated using a 1064 nm laser (1.0 W cm^{-2}) for 300 s. After treatment with different protocols, we recorded the body weight and the tumor volume of each mouse daily. The tumor volume was obtained using the equation: volume (mm^3) = length × $width^2/2$. The mice were treated for half a mouth, then all the mice were killed. These excised tumors and major organs containing the liver, kidney, lung, heart, and spleen were harvested for hematoxylin and eosin (H&E). The stained sections were recorded employing the Leica TCS SP8 instrument.

In vivo biodistribution assay

Female BALB/c mice bearing mice (n = 3 per group) were i.v. injected with CS–DA@Ru NPs (100 μL, 2.0 mg mL^{-1}). Subsequently, the mice were killed at 3, 6, 12, and 24 h, 3, 7, and 14 d postinjection, and tumors and the main organs (kidney, lung, spleen, liver, and heart) were harvested and digested using nitric acid to conduct a biodistribution analysis. The Ru element content in each tissue was tested using inductively coupled plasma optical mass spectrometry (ICP-MS).

Results and discussion

Synthesis and characterization of CS–DA@Ru NPs

The design and fabrication of CS–DA@Ru NPs are presented in Scheme 1. First, CS–DA was synthesized through a condensation reaction with chondroitin 4-sulfate sodium salt (CS) and dopamine (DA). Dopamine with its catechol group can act as a reducing agent, which could reduce Ru(III) ions to form initial Ru NPs and help stabilize the produced Ru NPs.[33,34] The structure of CS–DA is shown in Fig. S1 (ESI†), and ^1H NMR was used to detect CS–DA (Fig. S2, ESI†). CS–DA reduced $RuCl_3$ into Ru NPs and then CS–DA@Ru NPs were prepared. Fig. 1a shows the FTIR analysis, and the peak at 1630 cm^{-1} in CS was assigned to the vibration of C=O, whereas the peak at 1645 cm^{-1} in CS–DA was assigned to the vibration of C=O. This result suggests that CS–DA was successfully synthesized. A broad band centered at 3400 cm^{-1} and the peak at 1250 cm^{-1} were attributed to the vibration of O–H and C–O in CS–DA, respectively, which were replaced by two new absorption peaks at 3358 and 1226 cm^{-1} in CS–DA@Ru NPs. This result indicates that there is coordination interaction between Ru NPs and the phenolic hydroxyl group. Transmission electron microscopy (TEM) images showed that the synthesized CS–DA@Ru NPs were uniformly spherical with a diameter of approximately 100 nm (Fig. 1b, and Fig. S3, ESI†). The XRD analysis indicated that CS–DA@Ru NPs were amorphous (Fig. S4, ESI†). As exhibited in Fig. 1c, the hydrodynamic particle size of CS–DA@Ru NPs was tested to be approximately 110 nm according to the measurement of dynamic light scattering (DLS), which was consistent with that of the TEM results. As shown in Fig. 1d, the zeta potentials of CS–DA, Ru(III), and CS–DA@Ru NPs were determined to be −20.3 mV, 33.6 mV, and −14.1 mV, respectively, suggesting that CS–DA@Ru NPs have good stability in aqueous solution. This result further reveals that the negative charge of CS–DA was distributed on the Ru NPs surface. X ray photoelectron spectroscopy (XPS) was used to determine the surface electronic states and elemental composition. As shown in Fig. 1e, the survey spectrum indicated the existence of C, O, and Ru elements in CS–DA@Ru NPs. As seen in the high-resolution O 1s spectrum (Fig. 1f), two peaks at 532.8 eV and 531.6 eV were assigned to the phenolic hydroxyl oxygen (–C–OH) and the carbonyl oxygen (C=O), respectively.[35] The peak at 533.6 eV was attributed to the hydroxyl oxygens that stabilize the Ru NPs by donating their electrons.[36] As displayed in Fig. 1g, the peak at 284.8 eV and 288.0 eV was related to C–C or C–H, while the peak at 288.0 eV was associated with O=C–NH.[37] The peaks at 284.2 eV and 286.2 eV corresponded to Ru(0) $3d_{5/2}$ and Ru(III) $3d_{3/2}$, respectively.[38,39] As shown in Fig. 1h, the peaks located at 462.3 eV and 484.3 eV were assigned to Ru(0) $3p_{5/2}$ and Ru(0) $3p_{3/2}$, respectively, while the peaks at 463.9 eV and 486.3 eV were attributed to Ru(0) $3p_{5/2}$ and Ru(III) $3p_{3/2}$, respectively,[40] suggesting the existence of

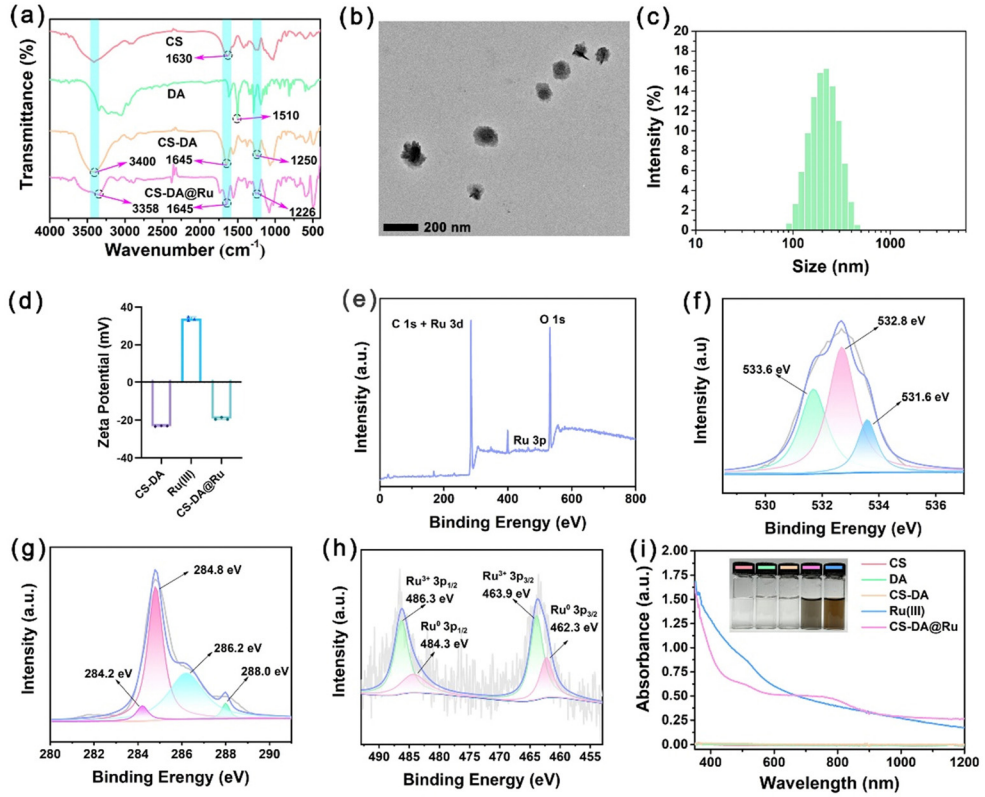

Fig. 1 Characterization of CS–DA@Ru NPs. (a) FTIR spectra of CS, DA, CS–DA, and CS–DA@Ru NPs. (b) TEM image of CS–DA@Ru NPs, scale bar is 200 nm. (c) Hydrodynamic diameter distribution of CS–DA@Ru NPs. (d) Zeta potential of CS–DA@Ru NPs. (e) Survey XPS spectrum of CS–DA@Ru NPs. (f) High-resolution O 1s spectrum of CS–DA@Ru NPs. (g) High-resolution C 1s and Ru 3d spectrum of CS–DA@Ru NPs. (h) High-resolution Ru 3p spectrum of CS–DA@Ru NPs. (i) UV-vis-NIR absorption spectra of CS, DA, CS–DA, Ru(III), and CS–DA@Ru NPs.

Ru(0). This result indicates that Ru(III) was successfully reduced to Ru(0) by dopamine. The ratio of Ru(III) : Ru(0) was equal to 2.28 : 1. CS–DA@Ru NPs exhibit broad absorption in the UV-vis-NIR region (Fig. 1i), suggesting that they may serve as a good photothermal agent candidate.

To estimate the stability of CS–DA@Ru NPs under physiological conditions, CS–DA@Ru NPs were dispersed in water, PBS, 1640, and DMEM, and treated for 0, 1, 3, 5, and 7 days, respectively. No obvious sediment was observed in the whole period (Fig. S5, ESI†). Particle dispersion index (PDI) values and hydrodynamic particle size of CS–DA@Ru NPs also exhibit no significant change after 7 days (Fig. S6, ESI†). These results indicate that CS–DA@Ru NPs exhibit excellent stability and dispersion under physiological conditions.

Photothermal performance and ROS generation capability of CS–DA@Ru NPs

Given the fact that the CS–DA@Ru NPs solution exhibited broad absorption in the NIR-II window (Fig. 1i), CS–DA@Ru NPs may serve as a NIR-II photothermal agent. The photothermal-conversion capability of the CS–DA@Ru NPs was estimated by irradiating the CS–DA@Ru NPs at various concentrations with a 1064 nm laser and the temperature changes were imaged using an IR camera. The photothermal heating curves confirmed that the temperature increase was dependent on the concentration of CS–DA@Ru NPs (Fig. 3a). The CS–DA@Ru NPs solution temperature increased to 56.7 °C under 1064 nm light irradiation for 10 min at a concentration of 200 μg mL^{-1} (Fig. 2a and b). In contrast, the temperature increase of pure water was negligible upon irradiation with the 1064 nm laser. The temperature of CS–DA@Ru NPs and pure water increased by 29 and 5 °C, respectively (Fig. 2c). These results suggest that the CS–DA@Ru NPs possess an excellent ability to convert the NIR-II light energy into thermal energy. The photothermal effect was also studied using the 1064 laser at different power densities, which increased with increasing power (Fig. S7, ESI†). The temperature exceeded 50 °C after 10 min of illumination at a power of 1.0 W cm^{-2}. Therefore, 1.0 W cm^{-2} power was used as the treatment power. The photothermal conversion efficiency (η) of CS–DA@Ru NPs was determined to be 29.24% (Fig. 2d). In addition, there were almost no changes in photothermal heating ability after five cycles of heating–cooling treatment, indicating exceptional photothermal stability of CS–DA@Ru NPs. Taken together, CS–DA@Ru NPs showed excellent photothermal performance.

To evaluate the CAT-like activity of CS–DA@Ru NPs, the ability of CS–DA@Ru NPs as nanozyme to catalyze H_2O_2 and produce O_2 was studied. We examined O_2 generation over 10 min using oxygen-dissolving equipment. As shown in Fig. 2f, the O_2 concentration has no obvious change in the H_2O_2 solution in the absence of CS–DA@Ru NPs. However, the

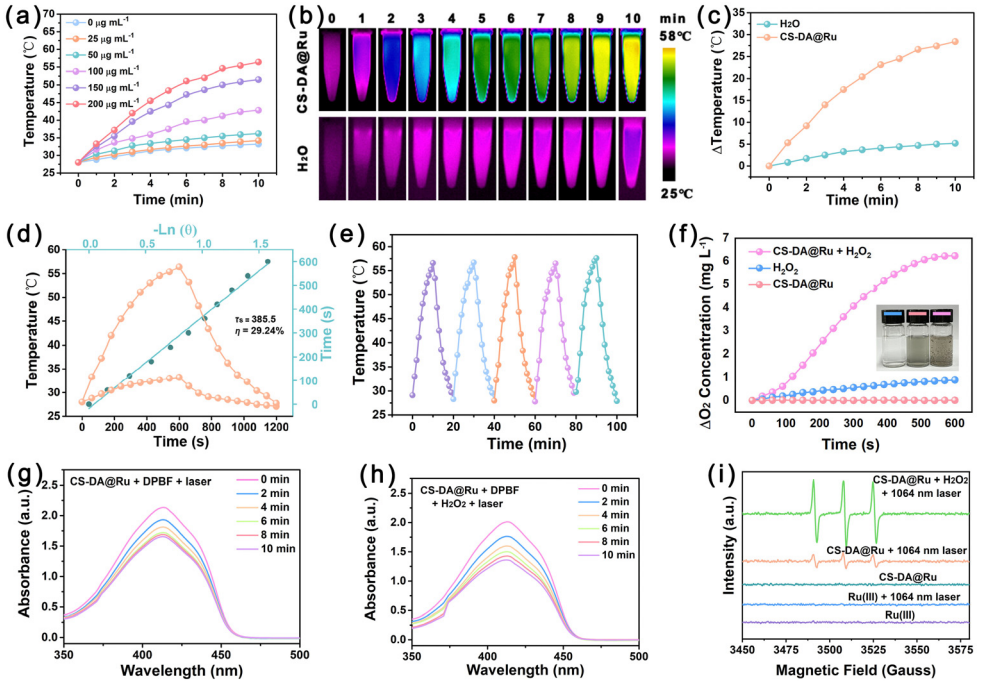

Fig. 2 Photothermal property and ROS generation capability of CS–DA@Ru NPs. (a) Temperature change curves of water and CS–DA@Ru NPs at various concentrations under 1064 nm light illumination. (b) Photographs of the CS–DA@Ru NPs solution (200 μg mL^{-1}) and H_2O under 1064 nm light illumination for 10 min, and (c) the corresponding increased temperature. (d) Photothermal heating and cooling curves of CS–DA@Ru NPs and water using 1064 nm light illumination for 10 min, followed by switching off the laser. Time constant (τ_s) obtained from the cooling period by utilizing the linear time data *versus* $-\ln\theta$. (e) Heating/cooling curves for five repeated ON–OFF cycles of laser irradiations. (f) Time-dependent O_2 generation curves of CS–DA@Ru NPs under different conditions. Inset: The corresponding pictures of different samples after 5 min of reaction. (g) UV-vis absorbance spectra of the DPBF solution treated with CS–DA@Ru NPs under 1064 nm light irradiation for different times. (h) UV-vis absorbance spectra of the DPBF solution treated with CS–DA@Ru NPs and H_2O_2 under 1064 nm light irradiation for different times. (i) EPR spectra of CS–DA@Ru NPs under various conditions in the presence of TEMP.

concentration of O_2 significantly increased with the addition of CS–DA@Ru NPs to the H_2O_2 solution, which suggested that CS–DA@Ru NPs possess excellent CAT-like activity. Subsequently, we investigated the $^1O_2$ generation production performance of CS–DA@Ru NPs under 1064 nm light illumination by DPBF, a singlet oxygen detection probe. As shown in Fig. 2g, the fluorescence intensity of DPBF was decreased with time prolonged in the presence of CS–DA@Ru NPs under 1064 nm laser illumination, suggesting the production of $^1O_2$. Furthermore, the addition of H_2O_2 could significantly increase the generation yield of $^1O_2$ (Fig. 2h), which was attributed to the CAT-like activity of CS–DA@Ru NPs catalyzing H_2O_2 to produce O_2 and enhance $^1O_2$ generation under 1064 nm laser irradiation. In contrast, the fluorescence intensity of DPBF treated with CS–DA@Ru NPs without laser irradiation or only irradiation with a laser in the absence of CS–DA@Ru NPs has no obvious decrease (Fig. S8, ESI†). By using TEMP as the $^1O_2$ trapping agent, the EPR spectra also demonstrated that H_2O_2 increased $^1O_2$ generation (Fig. 2i). As a result, CS–DA@Ru NPs have CAT-like activity and could enhance $^1O_2$ production under 1064 nm laser irradiation.

Cytotoxicity and intracellular therapeutic effects

By virtue of the splendid performance of CS–DA@Ru NPs in generating hyperthermia and cytotoxic ROS *via* a photodynamic process by modulating TME, *in vitro* therapeutic efficacy mediated by CS–DA@Ru NPs was further evaluated. First, the biocompatibility of CS–DA@Ru NPs was estimated using the standard MTT assay after the administration of CS–DA@Ru NPs against L929 murine fibroblast normal cells, 4T1 murine breast cancer cells, and HeLa human cervical cancer cells for 24 h. As shown in Fig. 3a, cell viability exceeded 70% even at a high CS–DA@Ru NPs concentration of 200 μg mL^{-1}, suggesting negligible cytotoxicity toward HeLa, 4T1, and L929 cells. This result demonstrates that CS–DA@Ru NPs could be used for *in vivo* antitumor applications. Subsequently, the targeting ability of CS–DA@Ru NPs was determined *via* ICP-MS. As shown in Fig. 3b, as the incubation time increased, the Ru concentration in 4T1 and HeLa increased, reaching its maximum at approximately 6 h. To further confirm the cellular uptake ability of CS–DA@Ru NPs, 4T1 and HeLa pretreated with CS for 2 h in advance, which allowed CS to occupy the target site of the CD44 protein and block the endocytosis of CS–DA@Ru NPs. The Ru concentration in HeLa and 4T1 cells pretreated with CS was lower than that in 4T1 and HeLa without pre-treatment. The same result was observed in L929 cells owing to their lack of surface CD44 protein. These results indicate that CS–DA@Ru NPs have good actively targeting ability to overexpress the CD44 protein of cancer cells and provide an optimal incubation time for subsequent cell experiments. As for the cytotoxicity assay of L929, 4T1, and HeLa cells against CS–DA@Ru NPs under 1064 nm laser irradiation, the

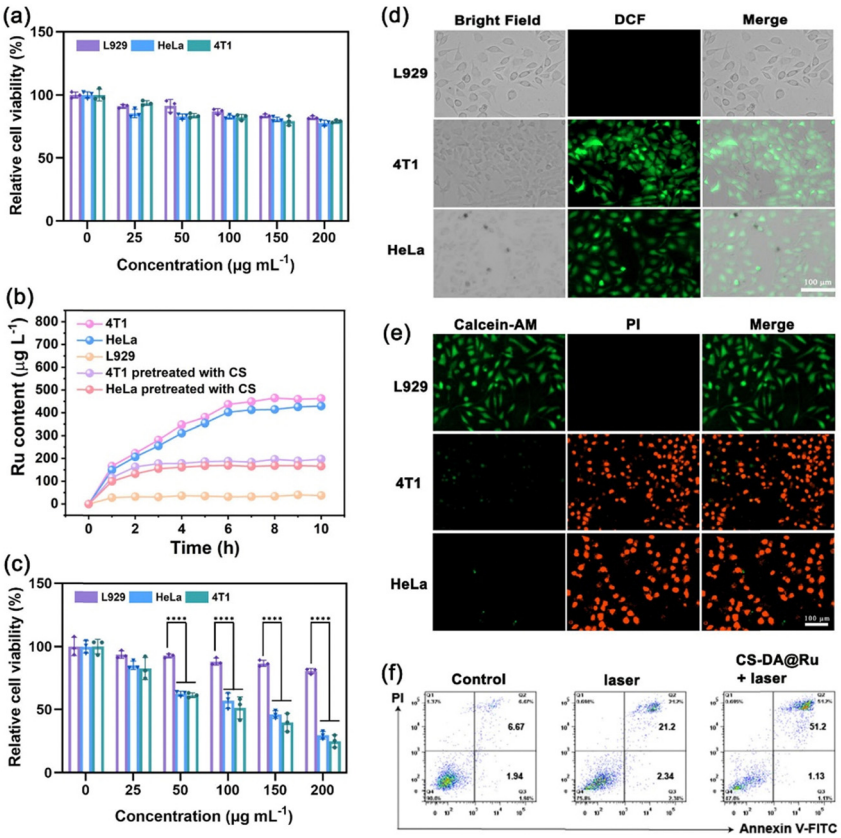

Fig. 3 CS–DA@Ru NPs-mediated cytotoxicity analysis *in vitro*. (a) Cell viability of L929, HeLa and 4T1 cells after incubation with gradient dosages of CS–DA@Ru NPs for 24 h. (b) L929, HeLa and 4T1 cells treated with CS–DA@Ru NPs (200 μg mL^{-1}) for different times, and HeLa and 4T1 cells pretreated with CS for 2 h after incubation with CS–DA@Ru NPs for different times. (c) Cell viability of L929, HeLa and 4T1 cells after incubation with various concentrations of CS–DA@Ru NPs for 4 h and irradiation with 1064 nm light for 300 s. (d) Fluorescence images of the intracellular ROS level in 4T1, HeLa and L929 cells stained with DCFH-DA after being treated with CS–DA@Ru NPs and irradiated using a 1064 nm laser for 5 min. Scale bar is 100 μm. (e) Fluorescence images of L929, HeLa and 4T1 cells stained with propidium iodide (red, dead cells) and calcein-AM (green, live cells) after being treated with CS–DA@Ru NPs and irradiated using 1064 nm light for 5 min. Scale bar is 100 μm. (f) Flow cytometry apoptosis analysis of 4T1 cells stained by PI and Annexin V-FITC after different treatments.

cytotoxicity increased with a higher concentration of CS–DA@Ru NPs toward these three cell lines. As shown in Fig. 3c, the cell viability of 4T1 and HeLa cells treated with CS–DA@Ru NPs (200 μg mL^{-1}) under 1064 nm light illumination was below 25%, probably owing to the combination of PTT/PDT of CS–DA@Ru NPs. The 4T1 and HeLa cells were induced toward apoptosis by enormous intracellular $^1O_2$ generation and local hyperthermia. In contrast, the cell viability of L929 cells was high under the same conditions. The result can be attributed to the surface of L929 cells lack of CD44 protein decreasing intake of CS–DA@Ru NPs. Furthermore, the production of ROS in 4T1 and HeLa cells incubated with CS–DA@Ru NPs was estimated using the DCFH-DA probe. The $^1O_2$ could react with DCFH-DA to produce green fluorescence of 2,7-dichlorofluorescein (DCF). As shown in Fig. 3d, no green fluorescence was seen in L929 cells incubated with CS–DA@Ru NPs. However, the HeLa and 4T1 cells incubated with CS–DA@Ru NPs displayed strong green fluorescence. The intracellular ROS generation of 4T1 cells was analyzed *via* flow cytometry (Fig. S9, ESI†). 4T1 cells incubated with CS–DA@Ru NPs under 1064 nm laser irradiation produced large amounts of ROS. This result was attributed to the overexpressed CD44 protein of cancer cells, increasing the uptake of CS–DA@Ru NP owing to the high affinity between CS and CD44 protein.

The cancer cell killing effect of CS–DA@Ru NP under 1064 nm laser illumination was assessed using a calcein-AM (green) and propidium iodide (red) double-staining assay. As shown in Fig. 3e, a strong and homogeneous green fluorescence was observed in L929 cells incubated with CS–DA@Ru NPs under 1064 nm laser irradiation, indicating that L929 cells were alive. However, a large area of red was seen in 4T1 and HeLa cells treated under the same conditions, suggesting that most 4T1 and HeLa cells were dead. This result indicates that CS–DA@Ru NPs under 1064 nm light irradiation could effectively kill cancer cells by PTT/PDT. Moreover, the flow cytometric apoptosis assay was employed to evaluate the 4T1 cell death after being stained with propidium iodide (PI) and Annexin V-FITC. As shown in Fig. 3f, the apoptotic ratio induced by CS–DA@Ru NPs using 1064 nm light illumination was 52.33% (Q2 + Q3), which is much higher than that of only 1064 nm light illumination (23.54%), which contains early apoptosis and late apoptosis. These *in vitro* results confirmed

that CS–DA@Ru NPs could effectively ablate cancer cells through synergistic PTT/PDT.

In vivo photoacoustic and photothermal imaging

In view of the strong NIR-II region absorbance and good photothermal properties of CS–DA@Ru NPs, we anticipated that CS–DA@Ru NPs could function as a good contrast-enhanced PA imaging nanomaterial and photothermal conversion agent for PTT. As shown in Fig. S10 (ESI†), *in vitro* PA images of CS–DA@Ru NPs display a good linearity between concentrations of CS–DA@Ru NPs and PA signal intensity, suggesting that CS–DA@Ru NPs were suitable for PA imaging. The cell experiment has proved that CS–DA@Ru NPs exhibit a high PA signal intensity. Based on the above data, CS–DA@Ru NPs were i.v. injected to the 4T1 tumor-bearing mice, and PA images were recorded at different times. As shown in Fig. 4a and b, as the time prolonged, the PA signal intensity of the tumor region gradually augmented and reached a maximum value at 12 h, suggesting the maximum accumulation of CS–DA@Ru NPs. Therefore, it can be inferred that the optimal laser illumination for treatment point is 12 h postinjection (i.v.) of CS–DA@Ru NPs. MSOT (multispectral optoacoustic tomography) could provide more efficient visualization through transfer multiple two-dimensional tomographic images to three-dimensional (3D) maximal intensity projection (MIP) images. The shape, size, location, and boundaries of the tumor can be clearly observed. The maximum PA signal was clearly seen at 12 h postinjection (i.v.) of CS–DA@Ru NPs through 3D imaging (Fig. 4c). The good *in vivo* PA-imaging ability of CS–DA@Ru NPs provides valuable guidance for subsequent treatment processes in mice.

It is known that the tumor microenvironment is hypoxic, which will decrease the treatment efficacy of O_2-dependent therapeutic methods such as PDT. To investigate whether CS–DA@Ru NPs can catalyze endogenous H_2O_2 to generate O_2 and alleviate tumor hypoxia, blood oxygen saturation was monitored in 4T1 tumor-bearing mice after i.v. administration of CS–DA@Ru NPs at different times by PA imaging. PA imaging is a

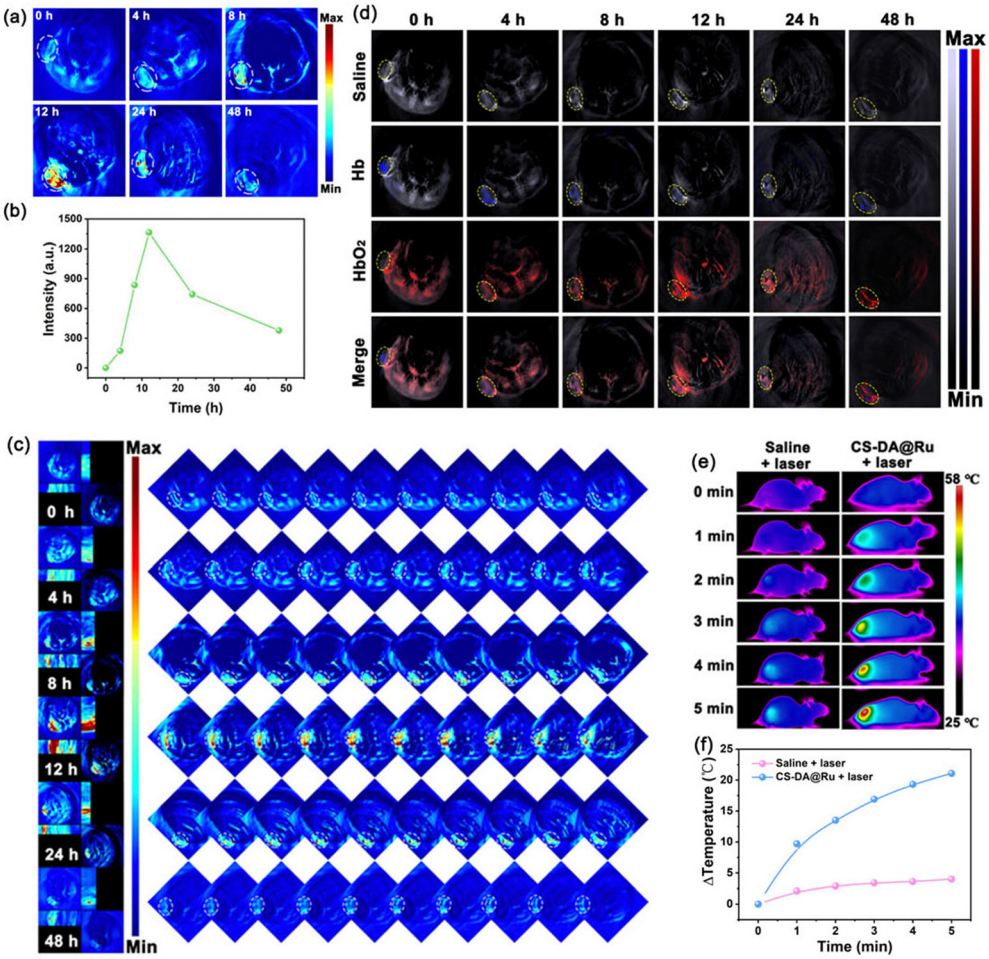

Fig. 4 *In vivo* imaging. (a) *In vivo* PA imaging of the tumor site after i.v. administration of CS–DA@Ru NPs at different time points. (b) The corresponding PA signal intensity. (c) Representative orthogonal-view 3D MOST images of the whole tumor area. (d) *In vivo* PA images of HbO_2 and Hb in mice after i.v. administration of CS–DA@Ru NPs at different times. (e) *In vivo* IR thermal images of the mice recorded at 12 h post-injection (i.v.) of CS–DA@Ru NPs under the 1064 nm laser irradiation for different times. (f) The corresponding temperature changes' curves recorded at 12 h post-injection (i.v.) of saline or CS–DA@Ru NPs under 1064 nm light illumination for different times.

typical method of real-time obtaining the oxygenation status according to the absorbance spectrum of deoxygenated hemoglobin (Hb) and oxygenated hemoglobin (HbO_2).[41] As seen in Fig. 4d, as the time increased, the PA signal of Hb was gradually decreased, while the PA signal of HbO_2 was gradually increased and reached a maximum at 12 h, indicating the accumulation of CS–DA@Ru NPs at the tumor site. In contrast, a weak PA signal was observed following i.v. injection of saline. These results confirmed that blood oxygen saturation dramatically increased owing to CS–DA@Ru NPs catalyzing H_2O_2 to generate O_2. Therefore, CS–DA@Ru NPs can elevate the $^1O_2$ level to enhance the therapeutic effect. Furthermore, the temperature change of the 4T1 tumor-bearing mice following i.v. administration of CS–DA@Ru NPs under 1064 nm laser irradiation was measured using an IR thermal camera. As exhibited in Fig. 4e, as for the mice treated with CS–DA@Ru NPs under 1064 nm irradiation for 5 min, the temperature of the tumor site increased to 57 °C with an elevation of 21 °C. In contrast, the temperature of the mice treated with the same volume of the saline + 1064 nm laser only increased by 3 °C. These results suggested that CS–DA@Ru NPs were suitable for *in vivo* treatment by PTT.

In vivo treatment effect of CS–DA@Ru NPs

On the basis of the confirmed desirable treatment efficiency of CS–DA@Ru NPs *in vitro*, the synergetic treatment effect of CS–DA@Ru NPs *in vivo* was investigated using 4T1 tumor-bearing BALB/c mice. Initially, the *in vivo* biodistribution was carried out to study the accumulation of CS–DA@Ru NPs. After the i.v. injection of CS–DA@Ru NPs at different time points, the tumors and main organs of mice were extracted and dissolved in nitric acid to monitor the Ru content using ICP-MS. As shown in Fig. 5a, it has been found that CS–DA@Ru NPs mainly accumulated in the liver and tumors. CS–DA@Ru NPs accumulated in the tumor due to the active targeting ability of CS to 4T1 cells and typical enhanced permeability and retention effect. It is a common phenomenon because the liver is an important delivery and transport organ. Furthermore, the liver displays rather high content of Ru, suggesting that CS–DA@Ru NPs may be quickly eliminated *via* liver metabolism.[42] Subsequently, we start evaluate the *in vivo* treatment effect of CS–DA@Ru NPs, which was performed by 4T1 tumor-bearing mice. After the volume of the tumor reached approximately 70 mm^3, 20 mice were divided into four groups (n = 5): (1) saline, (2) saline + laser, (3) CS–DA@Ru NPs, and (4) CS–DA@Ru NPs + laser. Saline and CS–DA@Ru NPs were i.v. injected into mice through the tail. The 1064 nm laser irradiated the tumor area at 12 h postinjection. During the 14 days of treatment, the tumor volume and body weight of each mouse were tested and recorded daily. As displayed in Fig. 5b, during the treatment period, the body weight change of mice in each group could be negligible, suggesting that the mice had good ability to tolerate the injection dose of CS–DA@Ru NPs. Both on the seventh and 14th days after the i.v. injection of mice with CS–DA@Ru NPs, the blood biochemistry assay results indicated that hepatic and renal function markers including creatinine (CREA), blood urea

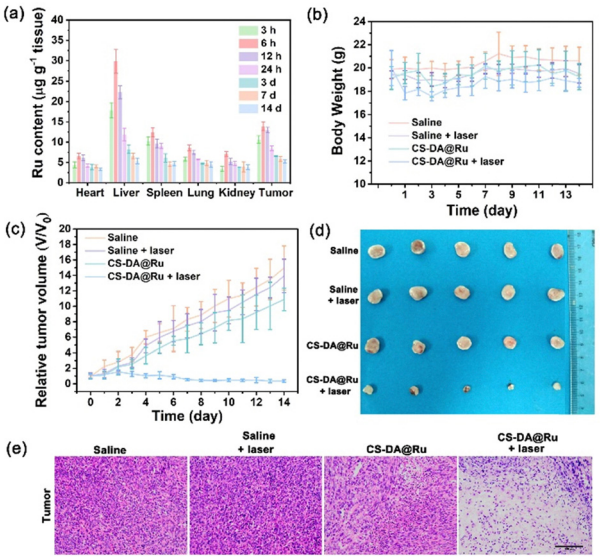

Fig. 5 Antitumor effect of CS–DA@Ru NPs *in vivo*. (a) The biodistribution of Ru in the tumor and main tissues at different times of postinjection of CS–DA@Ru NPs. (b) Body weight of mice in different treatment groups. (C) Relative tumor volume curves of mice with diverse treatments. (D) Digital photo of excised tumors in diverse groups after 14 days of treatment. (e) H&E staining of tumor tissues from each group after different treatments. Scale bar is 100 μm.

nitrogen (BUN), aspartate aminotransferase (AST) and alanine aminotransferase (ALT) exhibited no apparent changes compared with the saline group (Fig. S11, ESI†). From the blood routine assays, red blood cells (RBCs), mean corpuscular volume (MCV), mean corpuscular hemoglobin (MCH), white blood cells (WBCs), hemoglobin (HGB), mean corpuscular hemoglobin concentration (MCHC), hematocrit (HCT), and platelets (PLTs) were within normal reference ranges (Fig. S11, ESI†). Moreover, hematoxylin and eosin (H&E) staining of the major organs after treatment process was carried out. As exhibited in Fig. S12 (ESI†), there was no obvious damage to the major organs, indicating that the various treatments had long-term biosafety. As shown in Fig. 5c, the tumor growth of the mice i.v. administrated with CS–DA@Ru NPs plus 1064 nm laser illumination was significantly inhibited compared with mice in other groups. The inhibition effect was further demonstrated by the corresponding visualized pictures (Fig. 5d, and Fig. S13, ESI†). In addition, histopathological analysis was performed by H&E staining of the tumor tissue of mice after 14 days of treatment. As a result, the morphology of cells showed negligible damage in the saline, and saline + laser groups (Fig. 5e). In contrast, the tumor cells in the CS–DA@Ru NPs + laser group exhibited serious damage because of the changed cell shapes. Overall, these results confirmed that CS–DA@Ru NPs could effectively suppress tumor growth by PTT/PDT.

Conclusions

In summary, we have fabricated a self-supplying O_2 nanoplatform of CS–DA@Ru NPs for NIR-II PA imaging-guided

combination of PTT/PDT. The CS–DA@Ru NPs nanozyme exhibits good stability and dispersibility, splendid enzymatic activity, and photothermal properties. CS endowed CS–DA@Ru NPs with the ability to actively target cancer cells through CS–CD44 protein interactions. Moreover, CS–DA@Ru NPs with CAT activity effectively catalyze intracellular H_2O_2 into O_2 so as to relieve tumor hypoxia, which could augment the generation of $^1O_2$ under NIR-II laser irradiation. Furthermore, CS–DA@Ru NPs could generate enough hyperthermia and enormous amounts of $^1O_2$ under light irradiation. The tumor growth was effectively inhibited after a single injection of CS–DA@Ru NPs without negligible side effects. Overall, this finding provides an insight into the design of tumor-targeted, oxygen producing nanomaterials with augmented treatment efficacy for hypoxic tumors.

Conflicts of interest

There are no conflicts to declare.

Acknowledgements

The authors acknowledge financial support from the National Natural Science Foundation of China (Grant no. 21977022, 21865005, 22377018, and 22365007) and the National College Students' innovation and entrepreneurship training program (202310602009).

Notes and references

1 Z. Xie, T. Fan, J. An, W. Choi, Y. Duo, Y. Ge, B. Zhang, G. Nie, N. Xie, T. Zheng, Y. Chen, H. Zhang and J. S. Kim, Emerging combination strategies with phototherapy in cancer nanomedicine, *Chem. Soc. Rev.*, 2020, **49**, 8065–8087.

2 Q. Zheng, X. Liu, Y. Zheng, K. W. K. Yeung, Z. Cui, Y. Liang, Z. Li, S. Zhu, X. Wang and S. Wu, The recent progress on metal–organic frameworks for phototherapy, *Chem. Soc. Rev.*, 2021, **50**, 5086–5125.

3 S. S. Lucky, K. Chee and Y. Zhang, Nanoparticles in photodynamic therapy, *Chem. Rev.*, 2015, **115**, 1990–2042.

4 L.-H. Fu, Y. Wan, C. Li, C. Qi, T. He, C. Yang, Y. Zhang, J. Lin and P. Huang, Biodegradable calcium phosphate nanotheranostics with tumor-specific activatable cascade catalytic reactions-augmented photodynamic therapy, *Adv. Funct. Mater.*, 2021, **31**, 2009848.

5 H.-B. Cheng, H. Dai, X. Tan, H. Li, H. Liang, C. Hu, M. Huang, J. Y. Lee, J. Zhao, L. Zhou, Y. Wang, L. Zhang and J. Yoon, A facile, protein-derived supramolecular theranostic strategy for multimodal-imaging-guided photodynamic and photothermal immunotherapy in vivo, *Adv. Mater.*, 2022, **34**, 2109111.

6 Z. Tang, Y. Liu, M. He and W. Bu, Chemodynamic Therapy: Tumour Microenvironment-Mediated Fenton and Fenton-like Reactions, *Angew. Chem. Int. Ed.*, 2019, **58**, 946–956.

7 C. Zhang, K. Zhao, W. Bu, D. Ni, Y. Liu, J. Feng and J. Shi, Marriage of scintillator and semiconductor for synchronous radiotherapy and deep photodynamic therapy with diminished oxygen dependence, *Angew. Chem.*, 2015, **127**, 1790–1794.

8 R. Xu, Y. Wang, X. Duan, K. Lu, D. Micheroni, A. Hu and W. Lin, Nanoscale metal-organic frameworks for ratiometric oxygen sensing in live cells, *J. Am. Chem. Soc.*, 2016, **138**, 2158–2161.

9 L. Jiang, H. Bai, L. Liu, F. Lv, X. Ren and S. Wang, Luminescent, oxygen-supplying, hemoglobin-linked conjugated polymer nanoparticles for photodynamic therapy, *Angew. Chem. Int. Ed.*, 2019, **58**, 10660–10665.

10 D. Xia, D. Hang, Y. Li, W. Jiang, J. Zhu, Y. Ding, H. Gu and Y. Hu, Au−hemoglobin loaded platelet alleviating tumor hypoxia and enhancing the radiotherapy effect with low-dose X-ray, *ACS Nano*, 2020, **14**, 15654–15668.

11 S. Gao, Y. Jin, K. Ge, Z. Li, H. Liu, X. Dai, Y. Zhang, S. Chen, X. Liang and J. Zhang, Self-supply of O_2 and H_2O_2 by a nanocatalytic medicine to enhance combined chemo/chemodynamic therapy, *Adv. Sci.*, 2019, **6**, 1902137.

12 P. Zhu, Y. Chen and J. Shi, Nanoenzyme-augmented cancer sonodynamic therapy by catalytic tumor oxygenation, *ACS Nano*, 2018, **12**, 3780–3795.

13 L. He, Q. Ni, J. Mu, W. Fan, L. Liu, Z. Wang, L. Li, W. Tang, Y. Liu, Y. Cheng, L. Tang, Z. Yang, Y. Liu, J. Zou, W. Yang, O. Jacobson, F. Zhang, P. Huang and X. Chen, Solvent-assisted self-assembly of a metal–organic framework based biocatalyst for cascade reaction driven photodynamic therapy, *J. Am. Chem. Soc.*, 2020, **142**, 6822–6832.

14 Z. Tang, Y. Liu, M. He and W. Bu, Chemodynamic therapy: Tumour microenvironment-mediated Fenton and Fenton-like reactions, *Angew. Chem. Int. Ed.*, 2019, **58**, 946.

15 S. Dong, Y. Dong, B. Liu, J. Liu, S. Liu, Z. Zhao, W. Li, B. Tian, R. Zhao, F. He, S. Gai, Y. Xie, P. Yang and Y. Zhao, Guiding transition metal-doped hollow cerium tandem nanozymes with elaborately regulated multi-enzymatic activities for intensive chemodynamic therapy, *Adv. Mater.*, 2022, **34**, 2107054.

16 S. Dong, Y. Dong, T. Jia, S. Liu, J. Liu, D. Yang, F. He, S. Gai, P. Yang and J. Lin, GSH-depleted nanozymes with hyperthermia-enhanced dual enzyme-mimic activities for tumor nanocatalytic therapy, *Adv. Mater.*, 2020, **32**, 2002439.

17 W. Fan, W. Bu, B. Shen, Q. He, Z. Cui, Y. Liu, X. Zheng, K. Zhao and J. Shi, Intelligent MnO_2 nanosheets anchored with upconversion nanoprobes for concurrent pH-/H_2O_2-responsive UCL imaging and oxygen-elevated synergetic therapy, *Adv. Mater.*, 2015, **27**, 4155–4161.

18 Q. Jia, J. Ge, W. Liu, X. Zheng, S. Chen, Y. Wen, H. Zhang and P. Wang, A magnetofluorescent carbon dot assembly as an acidic H_2O_2-driven oxygenerator to regulate tumor hypoxia for simultaneous bimodal imaging and enhanced photodynamic therapy, *Adv. Mater.*, 2018, **30**, 1706090.

19 J. Sun, J. Wang, W. Hu, Y. Wang, Q. Zhang, X. Hu, T. Chou, B. Zhang, C. Gallaro, M. Halloran, L. Liang, L. Ren and H. Wang, A porous bimetallic Au@Pt core−shell oxygen

generator to enhance hypoxia dampened tumor chemotherapy synergized with NIR-II photothermal therapy, *ACS Nano*, 2022, **16**, 10711–10728.

20 H.-G. Fu, Y. Chen, Q. Yu and Y. Liu, A tumor-targeting Ru/polysac charide/protein supramolecular assembly with high photodynamic therapy ability, *ACS Nano*, 2022, **16**, 10711–10728.

21 Z. Xiao, X. Jiang, B. Li, X. Liu, X. Huang, Y. Zhang, Q. Ren, J. Luo, Z. Qina and J. Hu, Hydrous RuO_2 nanoparticles as an efficient NIR-light induced photothermal agent for ablation of cancer cells in vitro and in vivo, *Nanoscale*, 2015, **7**, 11962–11970.

22 L. Zeng, P. Gupta, Y. Chen, E. Wang, L. Ji, H. Chao and Z.-S. Chen, The development of anticancer ruthenium(II) complexes: From single molecule compounds to nanomaterials, *Chem. Soc. Rev.*, 2017, **46**, 5771.

23 W.-L. Wang, Z. Guo, Y. Lu, X.-C. Shen, T. Chen, R.-T. Huang, B. Zhou, C. Wen, H. Liang and B.-P. Jiang, Receptor-mediated and tumor-microenvironment Combination-responsive Ru nanoaggregates for enhanced cancer phototheranostics, *ACS Appl. Mater. Interfaces*, 2019, **11**, 17294–17305.

24 N. Meng, P. Xu, C. Wen, H. Liu, C. Gao, X.-C. Shen and H. Liang, Near-infrared-II-activatable sulfur-deficient plasmonic Bi_2S_{3-x}-Au heterostructures for photoacoustic imaging-guided ultrasound enhanced high performance phototherapy, *J. Colloid Interface Sci.*, 2023, **644**, 437–453.

25 P. Xu, C. Wen, C. Gao, H. Liu, Y. Li, X. Guo, X.-C. Shen and H. Liang, Near-infrared-II-activatable self-assembled manganese porphyrin-gold heterostructures for photoacoustic imaging-guided sonodynamic-augmented photothermal/photodynamic therapy, *ACS Nano*, 2024, **18**, 713–727.

26 C. Gao, W. Guo, X. Guo, Z. Ding, Y. Ding and X.-C. Shen, Black SnO_{2-x} based nanotheranostic for imaging-guided photodynamic/photothermal synergistic therapy in the second near-infrared window, *Acta Biomater.*, 2021, **129**, 220–234.

27 C. Zhou, L. Zhang, T. Sun, Y. Zhang, Y. Liu, M. Gong, Z. Xu, M. Du, Y. Liu, G. Liu and D. Zhang, Activatable NIR-II plasmonic nanotheranostics for efficient photoacoustic imaging and photothermal cancer therapy, *Adv. Mater.*, 2021, **33**, 2006532.

28 Y. Zhu, Z. Wang, R. Zhao, Y. Zhou, L. Feng, S. Gai and P. Yang, Pt decorated $Ti_3C_2T_x$ MXene with NIR-II light amplified nanozyme catalytic activity for efficient phototheranostics, *ACS Nano*, 2022, **16**, 3105–3118.

29 Y. Feng, X. Li, D. Ji, J. Tian, Q. Peng, Y. Shen and Y. Xiao, Functionalised penetrating peptide-chondroitin sulphate-gold nanoparticles: Synthesis, characterization, and applications as an anti-Alzheimer's disease drug, *Int. J. Biol. Macromol.*, 2023, **230**, 123125.

30 R. Sharma, K. Kuche, P. Thakor, V. Bhavana, S. Srivastava, N. K. Mehra and S. Jain, Chondroitin sulfate: Emerging biomaterial for biopharmaceutical purpose and tissue engineering, *Carbohydr. Polym.*, 2022, **286**, 119305.

31 N.-W. Kang, V. Visetvichaporn, D.-T. Nguyen, E. K. Shin, D.-H. Kim, M.-J. Kim, S.-Y. Yoo, J.-Y. Lee and D.-D. Kim, Bone tumor-homing nanotherapeutics for prolonged retention in tumor microenvironment and facilitated apoptotic process via mevalonate pathway inhibition, *Mater. Today Bio*, 2023, **19**, 100591.

32 H. Yu, H. Shi, M. Zhu, X. Zhang, L. Wang, G. Tian, L. Song, S. Luan, D. Qi and X. Chen, Salt-triggered adaptive dissociation coating with dual effect of antibacteria and anti-multiple encrustations in urological devices, *Adv. Healthcare Mater.*, 2023, **12**, 2203328.

33 S. Du, Y. Luo, Z. Liao, W. Zhang, X. Li, T. Liang, F. Zuo and K. Ding, New insights into the formation mechanism of gold nanoparticles usingdopamine as a reducing agent, *J. Colloid Interface Sci.*, 2018, **523**, 27.

34 M. Wang, S. Dai, N. Gan and Y. Wang, In situ growth of silver nanoparticles on polydopamine-coated chalcogenide glass tapered fiber for the highly sensitive detection of volatile organic compounds in water, *J. Non-Cryst. Solids*, 2022, **581**, 121420.

35 J. Ma, X. Huang, X. Liao and B. Shi, Preparation of highly active heterogeneous Au@Pd bimetallic catalyst using plant tannin grafted collagen fiber as the matrix, *J. Mol. Catal. A: Chem.*, 2013, **366**, 8–16.

36 H. Mao, C. Chen, X. Liao and B. Shi, Catalytic hydrogenation of quinoline over recyclable palladium nanoparticles supported on tannin grafted collagen fibers, *J. Mol. Catal. A: Chem.*, 2011, **341**, 51–56.

37 L. Fu and L. Cai, Ru nanoparticles loaded on tannin immobilized collagen fibers for catalytic hydrolysis of ammonia borane, *Int. J. Hydrogen Energy*, 2021, **46**, 1074–3762.

38 W. Chen, H. Li, J. Song, Y. Zhao, P. Ma, J. Niu and J. Wang, Binuclear Ru(III)-containing polyoxometalate with efficient photocatalytic activity for oxidative coupling of amines to imines, *Inorg. Chem.*, 2022, **61**, 2076–2085.

39 X. Yang, J. Wei, Q. Wang, M. Shuai, G. Yue, P. Li, D. Huang, D. Astruc and P. Zhao, Pd–Ru nanocatalysts derived from a Pd-induced aerogel for dramatic boosting of hydrogen release, *Nanoscale*, 2020, **12**, 2345.

40 J. Chen, H. Wang, Y. Gong and Y. Wang, Directly immobilizing a Ru–tannic acid linkage coordination complex on carbon cloth: An efficient and ultrastable catalyst for the hydrogen evolution reaction, *J. Mater. Chem. A*, 2019, **7**, 11038.

41 S. Liang, X. Deng, Y. Chang, C. Sun, S. Shao, Z. Xie, X. Xiao, P. Ma, H. Zhang, Z. Cheng and J. Lin, Intelligent hollow Pt-CuS janus architecture for synergistic catalysis-enhanced sonodynamic and photothermal cancer therapy, *Nano Lett.*, 2019, **19**, 4134–4145.

42 Y. Zhu, Z. Wang, R. Zhao, Y. Zhou, L. Feng, S. Gai and P. Yang, Pt decorated $Ti_3C_2T_x$ MXene with NIR-II light amplified nanozyme catalytic activity for efficient phototheranostics, *ACS Nano*, 2022, **16**, 3105–3118.

